Mechanical behavior and localized failure modes in a porous basalt from the Azores

S. Loaiza,[1] J. Fortin,[1] A. Schubnel,[1] Y. Gueguen,[1] S. Vinciguerra,[2] and M. Moreira[3]

Received 20 July 2012; revised 7 September 2012; accepted 9 September 2012; published 11 October 2012.

[1] Basaltic rocks are the main component of the oceanic upper crust, thus of potential interest for water and geothermal resources, storage of CO_2 and volcanic edifice stability. In this work, we investigated experimentally the mechanical behavior and the failure modes of a porous basalt, with an initial connected porosity of 18%. Results were acquired under triaxial compression experiments at confining pressure in the range of 25–200 MPa on water saturated samples. In addition, a purely hydrostatic test was also performed to reach the pore collapse critical pressure P*. During hydrostatic loading, our results show that the permeability is highly pressure dependent, which suggests that the permeability is mainly controlled by pre-existing cracks. When the sample is deformed at pressure higher than the pore collapse pressure P*, some very small dilatancy develops due to microcracking, and an increase in permeability is observed. Under triaxial loading, two modes of deformation can be highlighted. At low confining pressure (Pc < 50 MPa), the samples are brittle and shear localization occurs. For confining pressure > 50 MPa, the stress-strain curves are characterized by strain hardening and volumetric compaction. Stress drops are also observed, suggesting that compaction may be localized. The presence of compaction bands is confirmed by our microstructure analysis. In addition, the mechanical data allows us to plot the full yield surface for this porous basalt, which follows an elliptic cap as previously observed in high porosity sandstones and limestones. **Citation:** Loaiza, S., J. Fortin, A. Schubnel, Y. Gueguen, S. Vinciguerra, and M. Moreira (2012), Mechanical behavior and localized failure modes in a porous basalt from the Azores, *Geophys. Res. Lett.*, *39*, L19304, doi:10.1029/2012GL053218.

1. Introduction

[2] The understanding of a wide range of geophysical problems requires the knowledge of the mechanical properties of basalt, because they are the main component of the oceanic crust. The prediction of the failure modes, mechanical strength, porosity evolution and elastic moduli are of great importance in the geothermal energy production, CO_2 storage issues, water resources, and volcanic edifice stability [e.g., *Bredehoeft and Norton*, 1990; *d'Ozouville et al.*, 2008; *Goldberg et al.*, 2008; *Adelinet et al.*, 2011].

[3] Shear localization or cataclastic flow is commonly observed on a rock deformed under an overall compressive loading and one of the parameters of the rock which controls its brittleness and ductility is the porosity [*Rutter and Hadizadeh*, 1991; *Wong et al.*, 1997]. In basaltic lava, the porosity can vary between 1 to 30% [*Franzson et al.*, 2001]. This range of porosity can be explained in terms of decreasing viscosity of the lava during cooling: while the main body of the lava is well above solidus and has the highest fluidity, gas exsolves and produces individual vesicles, which migrate rapidly towards the top of the lava flow where a cooling crust is formed due to rapid cooling. As a consequence, the rock at the bottom of the lava flow is characterized by a low porosity, whereas high porosity may be found at its top [*Franzson et al.*, 2001].

[4] Previous studies on the mechanical properties of basalt, performed at room temperature, have mainly focused on low porosity specimens and the brittle regime was investigated extensively [*Stanchits et al.*, 2006; *Benson et al.*, 2007; *Fortin et al.*, 2011]. *Shimada et al.* [1989] first reported experimental results on the brittle-ductile transition in a 7% porosity basalt. The question addressed in this paper is "what is the mechanical behavior and failure mode of porous basalts"?

[5] Whereas there is a lack of data on the mechanical behavior of porous basalt, the mechanical behavior of porous sandstone has been extensively investigated [*Wong et al.*, 1997; *Klein et al.*, 2001; *Baud et al.*, 2004; *Fortin et al.*, 2006]. The failure mode of a porous sandstone undergoes a transition from brittle faulting to cataclastic compaction with increases in effective pressure. Cataclastic compaction is commonly reported as a response to purely hydrostatic loading: under pressure, the pore space is initially tightened by elastic deformation, and then at a critical pressure the pores collapse due to grain crushing. At low confining pressure, with increasing the differential stress, a sample may show dilatancy and fail by strain softening and brittle faulting. In the transitional regime from brittle faulting to cataclastic compaction, compaction bands can occur. Compaction bands are localized structures of reduced porosity which develop perpendicular to the main compressive stress.

[6] The purpose of our work was to investigate the mechanical behavior and failure mode of a porous basalt from the Azores, with an initial porosity of 18%. A series of triaxial compression tests was performed at room temperature under fully water saturated conditions at confining pressure ranging from 25 to 200 MPa. A hydrostatic test was also performed to reach the critical pressure of pore collapse P*. The full yield envelope of this rock was determined using stress-strain mechanical data. In addition, the evolution of the permeability

[1]Laboratoire de Géologie, Ecole Normale Supérieure, UMR 8538, CNRS, Paris, France.
[2]Dipartimento di Scienze della Terra, Università di Torino, Turin, Italy.
[3]Instituto Superior de Engenharia de Lisboa, Lisbon, Portugal.

Corresponding author: J. Fortin, Laboratoire de Géologie, Ecole Normale Supérieure, UMR 8538, CNRS, 24 Rue Lhomond, F75005 Paris, France. (fortin@geologie.ens.fr)

0094-8276/12/2012GL053218

Table 1. Chemical Composition of Sao Miguel 18% Porosity Basalt[a]

Na_2O (%)	MgO (%)	Al_2O_3 (%)	Si_2O (%)	K_2O (%)	CaO (%)	Ti_2O (%)	Fe0 (%)
5,33	1,85	17,63	58,67	5,65	5,07	1,53	4,28

[a]Data are expressed in oxide weight percentage.

was also measured during hydrostatic loading. Microstructural observations done on samples deformed in the different failure modes show that compaction bands occur in the transitional regime from brittle faulting to cataclastic compaction. The difference and similitude with the mechanical and failure modes in porous sandstones are discussed.

2. Sample and Experimental Set-Up

[7] Our basalt was extracted from a quarry in the island of Sao Miguel, Azores, Portugal. It is a microlitic alkali basalt with an initial connected porosity of 18% -measured by mercury porosimetry- and characterized by an initial permeability of 2.7 10^{-15} m². The mean pore entry diameter obtained from mercury porosimetry is 200 μm, and the mean size of the pore diameter from thin section analysis is about 500 μm. The matrix is characterized by a microlitic texture and the mean size of the grain is about 50 μm. The chemical composition of the microlitic matrix is presented in Table 1 in oxide weight percentage.

[8] Cylindrical samples (30 mm in diameter and 60 mm in length) were cored out of a single block. The experiments were conducted in the conventional triaxial apparatus installed at the Laboratoire de Géologie of Ecole Normale Supérieure. All experiments were performed at room temperature, at a constant strain rate of 10^{-5} s^{-1}. The axial strain was measured externally using a displacement transducer mounted between the moving piston and the fixed upper platen. The jacketed samples were saturated with tap water and stressed under fully drained condition. The pore pressure was kept constant at 5 MPa and from the pore volume change the porosity evolution of the samples was deduced. The steady-state technique was used to measure the permeability along the main axis of compression. At the end of each experiment, the sample was carefully unloaded for microstructural analysis. More details of the experimental setup can be found in [*Fortin et al.*, 2005].

3. Experimental Data

[9] We will use the convention that compressive stresses and compactive strains are positive, and we will refer to the maximum and minimum (compressive) principal stress by σ_1 and σ_3, respectively. The differential stress is referred as $Q = \sigma_1 - \sigma_3$. The difference between the confining pressure ($P_c = \sigma_2 = \sigma_3$) and the pore pressure (P_p) is denoted as the "effective pressure" P_{eff}, and the effective mean stress is as $P = (\sigma_1 + 2\sigma_3)/3\text{-}P_p$.

3.1. Hydrostatic Loading

[10] Figure 1a illustrates the evolution of porosity change under hydrostatic condition. For effective pressures lower than 50 MPa, the mechanical response of this porous basalt is nonlinear. This can be explained by pre-existing cracks closure or the closure of the more compliant pores. From Figure 1a, the porosity of the cracks can be estimated to ~1.5%, in agreement with data obtained by *Adelinet et al.* [2010] on an Icelandic porous basalt. As the effective pressure is increased further, the sample reaches a point where it suddenly becomes more compliant, showing a dramatic increase in volumetric compaction. This inflection point P* occurs at en effective pressure of 222 MPa. The mechanical behavior of this porous basalt is similar to what is commonly observed on high porosity sandstones [*Zhang et al.*, 1990], and the critical pressure P* is attributed to the onset of the pore collapse (see section 4).

[11] The evolution of permeability during hydrostatic loading is displayed on Figure 1b. As the effective pressure increases from 0 to 200 MPa, the permeability decreases by more than two orders of magnitude: from 2.7 10^{-15} m^2 to 1.9 10^{-17} m². However, as the critical pressure P* is reached, the permeability evolution reverses and increases slightly from 1.9 10^{-17} m² to 4.5 10^{-17} m² as the effective pressure is increased from P* up to 280 MPa. These data

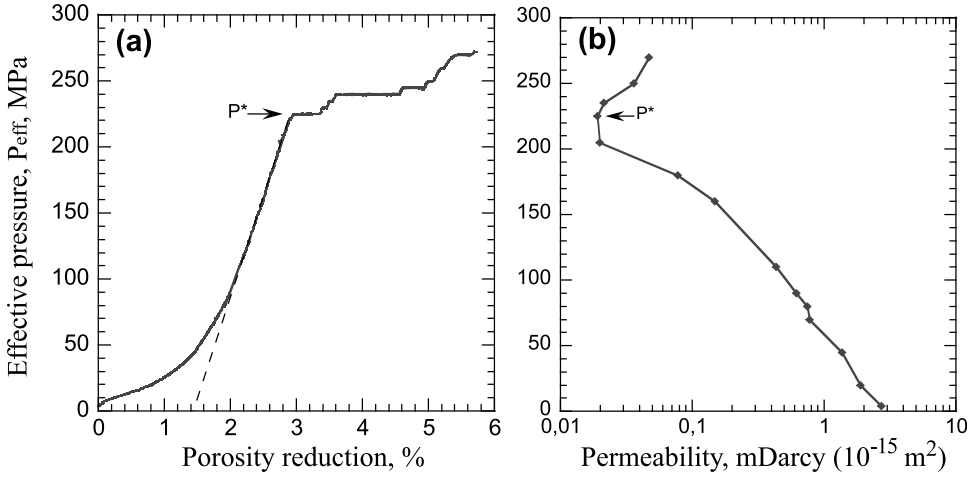

Figure 1. (a) Effective pressure as a function of porosity reduction. The onset of pore collapse P* is indicated by an arrow. (b) Permeability evolution as a function of effective pressure. Initial permeability is equal to 2.7 10^{-15} m². During hydrostatic loading, permeability decreased by two orders of magnitude. Beyond P*, inelastic compaction occurs and the permeability slightly increases.

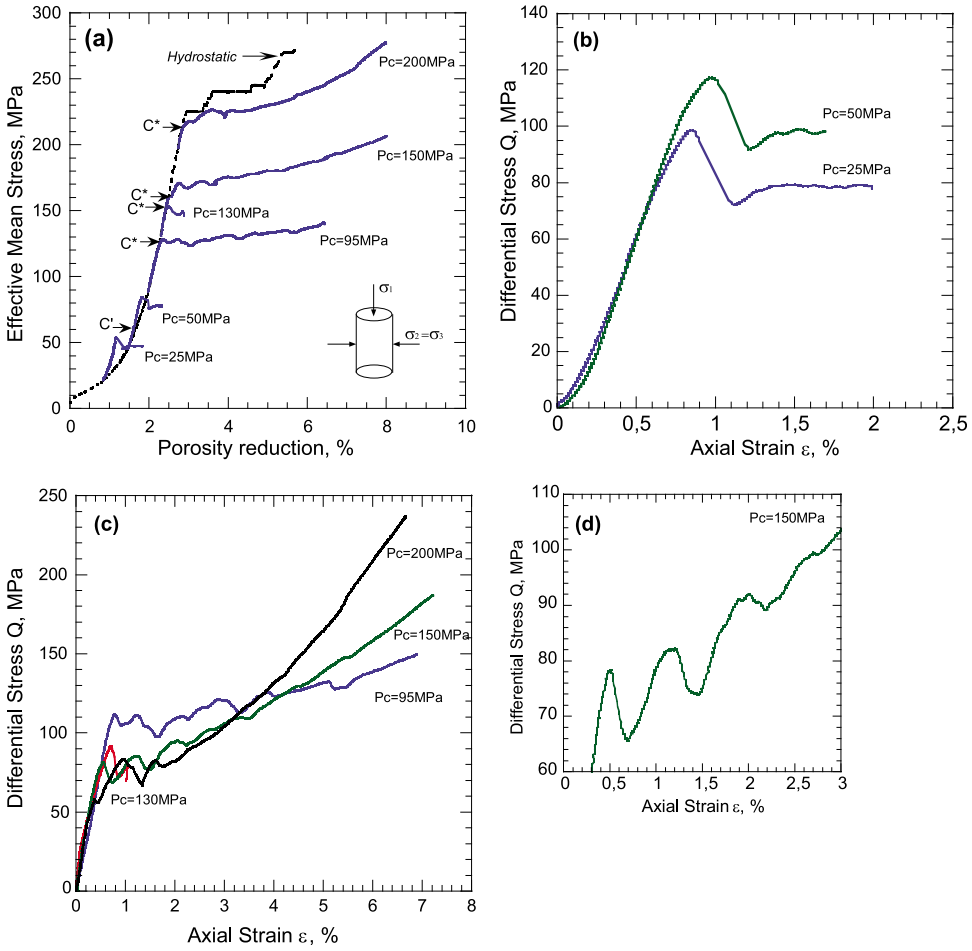

Figure 2. (a) Effective mean stress as a function of the porosity reduction during triaxial compression tests at fixed confining pressure as indicated (solid curves). For reference, the hydrostatic experiment is also plotted (dashed curve). The critical stress states C' and C* are indicated by arrows. (b) Differential stress versus axial strain for the experiment performed at Pc = 25 and 50 MPa. At these confining pressures, the samples failed by shear localization. (c) Differential stress versus axial strain for the experiment performed in the range of Pc = 95 to 200 MPa. At these confining pressures, the samples are ductile, but sharp stress drops can be observed, indicating that localized compaction may occur. (d) Zoom on the stress drops observed for the sample deformed at Pc = 150 MPa.

illustrating the complex relationship between porosity and permeability evolution during the compaction of a porous basalt will be discussed in section 5.2.

3.2. Triaxial Compression Experiments

[12] The porosity evolution versus the effective mean stress is given in Figure 2a. For confining pressure Pc = 25 and 50 MPa, the failure mode of this porous basalt is characterized by brittle deformation. The differential stress reaches a peak, beyond which strain softening is observed and the stress progressively drops to a residual level (Figure 2b). At the beginning of the triaxial loading, the porosity change coincides with the hydrostatic data up to a critical stress state –marked by the point C'- which marks the onset of shear-induced dilatancy [*Brace*, 1978; *Wong et al.*, 1997]. Beyond C' and before the peak stress is attained, the compaction decelerates in comparison to the hydrostat (dashed-line), which implies that the deviatoric stress field induces the pore space to dilate.

[13] For confining pressure between 95 and 200 MPa, the stress-strain curves are characterized by ductile attributes. Figure 2c shows the evolution of axial strain as a function of differential stress, showing an overall strain-hardening trend. Note that strain hardening is more pronounced as confining pressure increases, as expected. Figure 2a shows that the failure mode for this range of confining pressures is associated with an appreciable porosity reduction. The triaxial curve for a given effective pressure coincides with the hydrostat up to a critical stress state C*, however at stresses higher than C* the deviatoric stresses provide significant contribution to the compactive strain. This phenomenon is referred to as "shear-enhanced compaction" [*Wong et al.*, 1997] and is attributed in porous sandstones to the beginning of grain crushing and pore collapse [*Menéndez et al.*, 1996]. While a sample undergoes shear-enhanced compaction, Figures 2a and 2c also show that the overall hardening trend is punctuated by sharp stress drops of up to 20 MPa in amplitude. Figure 2d is a zoom of the differential stress – axial strain curve for the experiment performed at Pc = 150 MPa, where three distinct stress drops can be observed. These episodic stress drops may indicate that localized compaction, *i.e.* compaction bands, is occurring [*Klein et al.*, 2001]. The experiments performed at 95, 150,

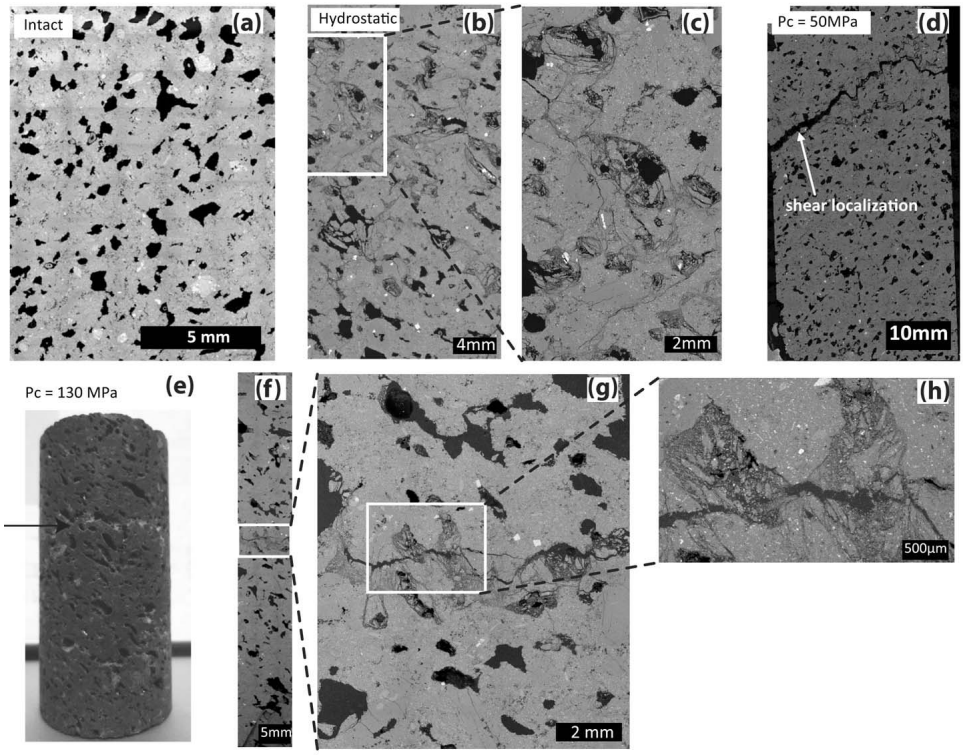

Figure 3. Microstructural analysis. (a) SEM micrograph of an intact sample: the pores appear in black. (b and c) SEM micrographs of the sample deformed hydrostatically, revealing pore collapse and damage around the pores surfaces. (d) Micrograph of the sample deformed at 50 MPa confining pressure. A shear failure, with an angle of about 45°, is clearly observed. (e) Picture of the sample deformed at 130 MPa confining pressure. A macroscopic compaction band, indicated by an arrow, can be observed clearly. (f–h) SEM micrographs of the sample deformed at 130 MPa confining pressure. A clear compaction band is observed in the middle part of the sample. Higher magnification images (Figures 3g and 3h) reveal details inside the compaction band such as pore collapse and induced cracking.

200 MPa were stopped at an axial strain of 7%, whereas the experiment performed at 130 MPa was stopped just after the first stress drop, *i.e.* for an axial strain of 1.1%. In addition, for the experiment performed at Pc = 130 MPa, the permeability was measured just before the deviatoric loading and just after the first stress drop occurred at an axial strain of 1.1%. We measured $k = 2.2\ 10^{-16}$ m² at 0 differential stress in agreement with Figure 1b, and $k = 3.6\ 10^{-17}$ m² just after the first stress drop.

4. Microstructural Observations

[14] Analysis of the microstructure was performed on intact and deformed samples using a Field Emission Scanning Electron Microscope (FE-SEM). To obtain SEM thin sections, samples were cut parallel to the specimen long axis and maximum compressive stress σ_1. Figure 3a is an SEM micrograph of an intact sample. The matrix appears in grey and pores in black. Note that mean pore diameter is 500 μm, but the pore diameter can vary from 1 to 900 μm.

[15] Figure 3b is a SEM micrograph of the sample compressed hydrostatically (Figure 1). Damage in this sample is primarily associated with pore collapse, and pore at various stages of collapse can be observed throughout the sample (Figures 3b and 3c). Fragments fill partially the pore space. Intensive damage is observed around the pores surfaces, which suggests that stress-induced cracks coalesce first around the pore surface. Moreover, Figure 3c shows that some stress-induced cracks coalesce from one collapsed pore to another, this observation tends to prove that stress-induced cracks form a newly connected porous network, which is consistent with the increase in permeability observed for pressures higher than P*.

[16] Figure 3d is a micrograph of the sample deformed in triaxial conditions at 50 MPa confining pressure. A shear band, with an angle of about 45°, can be clearly observed. Stress-induced cracks are mainly located in the zone of the shear failure. These observations are consistent with the mechanical data (Figure 2) and previous studies performed on low porosity basalts [*Stanchits et al.*, 2006].

[17] Figure 3e is a picture of the sample stressed at a confining pressure of 130 MPa. A strain localization band perpendicular to the main compressive axis, indicated by an arrow, is visible to the naked eye. To investigate in more details the microstructure, this sample was cut in four equal half. Figure 3f is an SEM micrograph obtained on the total length of the sample on a width of ~10 mm. One compaction band can be seen in the middle part of the sample. The band appears as a horizontal structure where the pores have collapsed. In this band of ~10 mm length, stress-induced cracks coalesce first at the pore surface and the fragments fill the pore space (Figure 3h). In addition, some induced cracks extend and coalesce with each other, mainly in the sub horizontal

direction, *i.e.* perpendicular to main axis compression stress. The thickness of the band is approximately 2 mm. Outside the band, Figure 3f shows that the microstructure of the rock remains intact. Following the terminology introduced by *Baud et al.* [2004], a localized structure that has a thickness of only a few grains is referred to as "discrete band", whereas thicker structure are called "diffuse bands". In this porous basalt, a compaction band seems to be "discrete" and not "diffuse". For the triaxial experiments performed at Pc = 95, 150, and 200 MPa, we reached a maximum axial strain of 7%. In these experiments, SEM micrographs show that, by then, almost all the sample has compacted so that the imprints of clear individual compaction bands has been lost in the microstructure. In addition, if it is clear for the experiment performed at 130 MPa, that one stress drop corresponds to one compaction band; more experiments stopped at different axial strain are needed to conclude on the correspondence between number of bands and stress drops.

5. Discussion and Conclusions

5.1. Envelopes for Brittle Strength and Compactive Yield

[18] Data for the brittle strength, the onset of dilatancy C' and onset of shear-enhanced compaction C* are showed on the P (effective mean stress) and Q (differential stress) space in Figure 4. For the brittle strength we have only two data (Pc = 25 and 50 MPa), thus the Mohr-Coulomb envelope remains unsettled. However, for the experiments performed at Pc ≥ 95 MPa, the onset of shear-enhanced compaction shows a negative pressure dependence, and the data map out an elliptical yield cap envelope of the form [*Wong et al.*, 1997]:

$$\frac{\left(\frac{P}{P^*}-\gamma\right)^2}{(1-\gamma)^2}+\frac{\left(\frac{Q}{P^*}\right)^2}{\delta^2}=1$$

with the critical pore collapse pressure P* = 222 MPa, and parameter values $\delta = 0.5$ and $\gamma = 0.29$. Such an elliptical cap envelope has been extensively observed in sandstones [*Wong et al.*, 1997] and limestones [*Vajdova et al.*, 2004a]. However, and to our knowledge, this is the first time it is observed in a porous basalt.

5.2. Evolution of the Permeability During the Hydrostatic Compaction

[19] The data (see section 3) obtained during the hydrostatic compaction of this porous basalt from the Azores illustrates the complex relationship between porosity and permeability evolution. Our experimental results show that cracks, although they represent less than 2% porosity - for a total porosity of 18% - may in fact control the permeability evolution with pressure. Indeed, the drastic permeability reduction of more than two orders of magnitude observed as effective pressure increases up to P* is similar to the measurements performed under pressure in low porosity Etna basalt [*Morrow et al.*, 1994; *Fortin et al.*, 2011], or even cracked glass [*Ougier-Simonin et al.*, 2011a, 2011b]. Previous published data [*David et al.*, 1994] show that for low-porosity rocks, permeability decreases exponentially with increasing effective pressure. The pressure sensitivity is quantified through a critical pressure P_k such that $k = k_0\, e^{-P/P_k}$. From Figure 1b, we estimate P_k = 11.7 MPa. This value is consistent with those previously reported for low porous basalt or granite [*Morrow et al.*, 1994; *David et al.*, 1994; *Fortin et al.*, 2011]. Such a high permeability sensivity to pressure contrasts with the usual behavior of high porosity rocks and highlights that the permeability of this porous basalt is mainly controlled by pre-existing cracks. This implies that for this porous basalt, the key parameter is not the porosity -mainly controlled by the amount of equant pores- but the connectivity between these pores, which is controlled by the cracks.

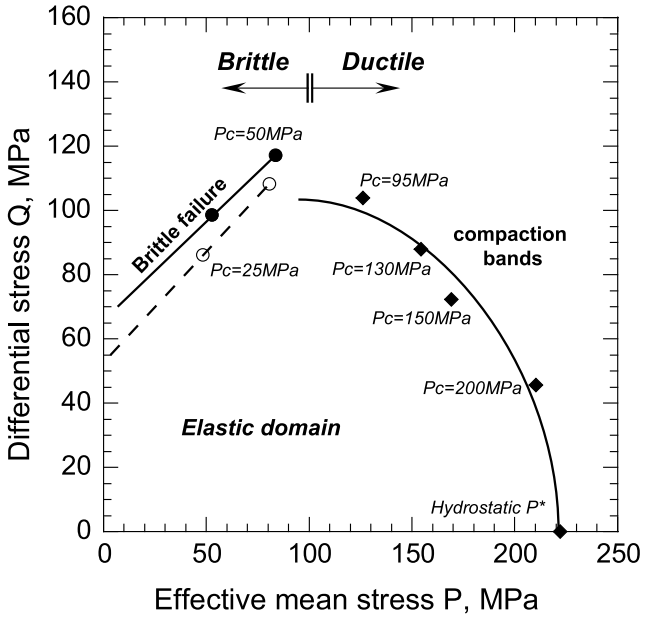

Figure 4. Yield envelopes for brittle strength and shear enhanced compaction: peak stress and stress states C' and C* are shown in the P-Q stress space. The compactive yield envelope approximately follows an ellipse.

[20] Cracks also seem to control the permeability evolution beyond the critical pressure P*. The critical pressure P* is the point where pore collapse takes place [*Zhang et al.*, 1990] which implies that cracking take places (see also section 4). The occurrence of cracking implies that limited amount of dilatancy also develops at P*. The porosity reduction resulting from pore collapse is larger than the dilatancy induced by microcrack propagation by at least one order of magnitude, so that dilatancy is not visible on Figure 1a. Its existence is, however, confirmed both by our microstructural observations (Figures 3b and 3c) and the permeability evolution, which increases for effective pressure higher than P*. This increase in permeability can only be due to the development of cracks, enhancing the hydraulic connectivity of the sample. This observation contrasts to what is observed in porous sandstones, where the critical pressure P* is generally associated with drastic decreases in permeability [*Zhu and Wong*, 1997; *Fortin et al.*, 2005].

5.3. Compaction Bands in a Basalt: Comparison With Observations Done in Porous Sandstone

[21] In our basalt, the formation of compaction bands is observed for Pc ≥ 95 MPa. Such structures were initially first observed in porous sandstones. However, there seem to be at least three important differences. First, compaction bands were only observed in sandstones with porosity higher than 24%

[*Baud et al.*, 2004]. The porosity of our basalt is only 18%, and compaction bands appear at relatively low confining pressures. Another parameter to be taken into account is the ratio between grain size and pore size [*Adelinet et al.*, 2012]. Indeed, for this basalt, the grain size is $\sim$50 μm (matrix microlites) and the mean pore diameter is $\sim$500 μm, leading to a ratio about 1:10, whereas a ratio of 10:1 is more commonly observed in sandstones. This ratio probably plays a role in the threshold values of critical stress needed to form compaction bands.

[22] Second, in sandstones, compaction bands appear as a zone of grain crushing and pore collapse [*Baud et al.*, 2004; *Stanchits et al.*, 2009]. In basalt however, a compaction band seems to be primarily the result of pore collapse. Cracks seem to coalesce first around the pore circumference, and then the fragments fill the pore space. A compaction band in basalt appears as the result of the collapse of several aligned pores in a direction perpendicular to the main compression axis. Its structure is closer to compaction bands that can be observed in porous material like honeycombs [*Papka and Kyriakides*, 1999] than to compaction bands in sandstones. Again, the difference in the ratio between grain size and pore size may explain such difference.

[23] In sandstones, a compaction band is a barrier for fluid flow [*Vajdova et al.*, 2004b]. In basalt, the effect of compaction bands on permeability is still unclear. For the experiment performed at Pc = 130 MPa, the permeability reduction between the beginning of the differential loading and just after the first stress drop is approximately of one order of magnitude. However, this permeability reduction may also be explained by the closure of pre-existing cracks in the undamaged parts of the sample during the loading, as it has been demonstrated that permeability was highly pressure sensitive. However, within a compaction band the permeability may increase because of the improved pore space connectivity. The overall balance is thus variable and more experiments are thus needed to conclude about the effect of compaction bands on the permeability in porous basalts.

[24] **Acknowledgments.** We thank T.-F. Wong and S. Stanchits for their comprehensive reviews of the manuscript. This work was partially founded by the FreeRock project funded by FCT (Portugal) and by the ANR Agency (GIIWS project). The authors would like to acknowledge the technical help of Damien Deldicque for SEM analysis.

[25] The Editor thanks Sergei Stanchits and Teng-Fong Wong for their assistance in evaluating this paper.

References

Adelinet, M., J. Fortin, Y. Gueguen, A. Schubnel, and L. Geoffroy (2010), Frequency and fluid effects on elastic properties of basalt: Experimental investigations, *Geophys. Res. Lett.*, *37*, L02303, doi:10.1029/2009GL041660.

Adelinet, M., C. Dorbath, M. Le Ravalec, J. Fortin, and Y. Gueguen (2011), Deriving microstrure and fluid state within the Icelandic crust from the inversion of tomography data, *Geophys. Res. Lett.*, *38*, L03305, doi:10.1029/2010GL046304.

Adelinet, M., J. Fortin, A. Schubnel, and Y. Gueguen (2012), Deformations modes in an Icelandic basalt: from brittle failure to localized deformation bands, *J. Volcanol. Geotherm. Res.*, in press.

Baud, P., E. Klein, and T.-F. Wong (2004), Compaction localization in porous sandstone: Spatial evolution of damage and acoustic emission activity, *J. Struct. Geol.*, *26*, 603–624.

Benson, P. M., B. D. Thompson, P. G. Meredith, S. Vinciguerra, and R. Young (2007), Imaging slow failure in triaxially deformed Etna basalt using 3D acoustic emission location and X-ray computed tomography, *Geophys. Res. Lett.*, *34*, L03303, doi:10.1029/2006GL028721.

Brace, W. F. (1978), Volume changes during fracture and frictional sliding: A review, *Pure Appl. Geophys.*, *116*, 603–614, doi:10.1007/BF00876527.

Bredehoeft, J. D., and D. L. Norton (Eds.) (1990), *The Role of Fluid in Crustal Processes*, 170 pp., Nat. Acad. Press, Washington, D. C.

d'Ozouville, N., E. Auken, K. Sorensen, S. Violette, G. De Marsily, B. Deffontaines, and G. Merlen (2008), Extensive perched aquifer and structural implications revealed by 3D resistivity mapping in a Galapagos volcano, *Earth Planet. Sci. Lett.*, *269*, 518–522, doi:10.1016/j.epsl.2008.03.011.

David, C., T. F. Wong, W. Zhu, and J. Zhang (1994), Laboratory measurements of compaction induced permeability change in porous rocks: Implications for the generation and maintenance of pore pressure excess in the crust, *Pure Appl. Geophys.*, *143*, 425–456, doi:10.1007/BF00874337.

Fortin, J., A. Schubnel, and Y. Guéguen (2005), Elastic wave velocities and permeability evolution during compaction of Bleurswiller sandstone, *Int. J. Rock Mech. Min. Sci.*, *42*, 873–889, doi:10.1016/j.ijrmms.2005.05.002.

Fortin J., S. Stanchits, G. Dresen, and Y. Gueguen (2006), Acoustic emission and velocities associated with the formation of compaction bands in sandstone, *J. Geophys. Res.*, *111*, B10203, doi:10.1029/2005JB003854.

Fortin, J., S. Stanchits, S. Vinciguerra, and Y. Gueguen (2011), Influence of thermal and mechanical cracks on permeability and elastic wave velocities in a basalt from Mt. Etna volcano subjected to elevate pressure, *Tectonophysics*, *503*, 60–74, doi:10.1016/j.tecto.2010.09.028.

Franzson, H., S. Þór Guðlaugsson, and G. O. Friðleifsson (2001), Petrophysical Properties of Icelandic Rocks, paper presented at 6th Nordic Symposium on Petrophysics, Nordic Energy Res. Programme, Trondheim, Norway.

Goldberg, D., T. Takahashi, and A. Slagle (2008), Carbon dioxide sequestration in deep-sea basalt, *Proc. Natl. Acad. Sci. U. S. A.*, *105*, 9920–9925, doi:10.1073/pnas.0804397105.

Klein, E., P. Baud, T. Reuschlé, and T.-F. Wong (2001), Mechanical behavior and failure mode of Bentheim sandstone under triaxial compression, *Phys. Chem. Earth Part A*, *26*, 21–25, doi:10.1016/S1464-1895(01)00017-5.

Menéndez, B., W. Zhu, and T.-F. Wong (1996), Micromechanics of brittle faulting and cataclastic flow in Berea sandstone, *J. Struct. Geol.*, *18*(1), 1–16, doi:10.1016/0191-8141(95)00076-P.

Morrow, C., D. Lockner, S. Hickman, M. Rusanov, and T. Röckel (1994), Effects of lithology and depth on the permeability of core samples from the kola and KTB drillholes, *J. Geophys. Res.*, *99*, 7263–7274, doi:10.1029/93JB03458.

Ougier-Simonin, A., J. Fortin, Y. Guéguen, A. Schubnel, and F. Bouyer (2011a), Cracks in glass under triaxial conditions, *Int. J. Eng. Sci.*, *49*(1), 105–121, doi:10.1016/j.ijengsci.2010.06.026.

Ougier-Simonin, A., Y. Gueguen, J. Fortin, A. Schubnel, and F. Bouyer (2011b), Permeability and elastic properties of cracked glass under pressure, *J. Geophys. Res.*, *116*, B07203, doi:10.1029/2010JB008077.

Papka, S. D., and S. Kyriakides (1999), Biaxial crushing of honeycombs - Part I: Experiments, *Int. J. Solids Struct.*, *36*, 4367–4396, doi:10.1016/S0020-7683(98)00224-8.

Rutter, A., and J. Hadizadeh (1991), On the influence of porosity on the low-temperature brittle—Ductile transition in siliciclastic rocks, *J. Struct. Geol.*, *13*(5), 609–614, doi:10.1016/0191-8141(91)90047-M.

Shimada, M., K. Ito, and A. Cho (1989), Ductile behavior of a fine-grained porous basalt at room temperature and pressure to 3 GPa, *Phys. Earth Planet. Inter.*, *55*, 361–373, doi:10.1016/0031-9201(89)90083-6.

Stanchits, S., S. Vinciguerra, and G. Dresen (2006), Ultrasonic velocities, acoustic emission characteristics and crack damage of basalt and granite, *Pure Appl. Geophys.*, *163*, 975–994, doi:10.1007/s00024-006-0059-5.

Stanchits, S., J. Fortin, G. Dresen, and Y. Gueguen (2009), Initiation and propagation of compaction bands in dry and wet Bentheim sandstone, *Pure Appl. Geophys.*, *166*, 843–868, doi:10.1007/s00024-009-0478-1.

Vajdova, V., P. Baud, and T.-F. Wong (2004a), Compaction, dilatancy and failure in porous carbonate rocks, *J. Geophys. Res.*, *109*, B05204, doi:10.1029/2003JB002508.

Vajdova, V., P. Baud, and T.-F. Wong (2004b), Permeability evolution during localized deformation in Bentheim sandstone, *J. Geophys. Res.*, *109*, B10406, doi:10.1029/2003JB002942.

Wong, T.-F., C. David, and W. Zhu (1997), The transition from brittle faulting to cataclastic flow in porous sandstone: Mechanical deformation, *J. Geophys. Res.*, *102*, 3009–3025, doi:10.1029/96JB03281.

Zhang, J., T.-F. Wong, and D. M. Davis (1990), Micromechanics of pressure-induced grain crushing in porous rocks, *J. Geophys. Res.*, *95*, 341–352, doi:10.1029/JB095iB01p00341.

Zhu, W., and T.-F. Wong (1997), The transition from brittle faulting to cataclastic flow in porous sandstone: Permeability evolution, *J. Geophys. Res.*, *102*, 3027–3041, doi:10.1029/96JB03282.